Int. J. Microgravity Sci. Appl., **33** (2) (2016) 330206
DOI: 10.15011/jasma.33.330206

IIIII ISPS-6 Proceedings IIIII
(Original Paper)

Preliminary Experiments Using Electromagnetic Levitation On the International Space Station

Douglas M. MATSON [1], Xiao XIAO [1], Justin RODRIGUEZ [1] and Rainer K. WUNDERLICH [2]

Abstract

Calibration and check-out runs during FeCrNi steel alloy melting cycles on the International Space Station are compared to previous test results from experimental platforms both in microgravity and on ground. Four key thermophysical properties are investigated: density, thermal expansion, surface tension and viscosity. Analysis shows that the three facilities yield results with comparable accuracy but the space results indicate that planned changes to on-orbit processing protocol are required to maximize the potential for significantly improved precision.

Keyword(s): Electromagnetic Levitation Processing, Thermophysical Property Measurement

Received 29 January 2016, Accepted 12 April 2016, Published 30 April 2016

1. Introduction

The Materials Science Laboratory ElectroMagnetic Levitator (MSL-EML) was launched by the European Space Agency (ESA) on ATV-5 and installed in the Columbus Module by astronaut/flight engineer Alexander Gerst during the International Space Station (ISS) Blue Dot Mission. Activation was successfully accomplished early in 2015 with calibration tests starting in February and continuing with preliminary levitation experiments throughout the remainder of the calendar year. The facility contains 18 samples in this the first of six batches supporting over ten international teams investigating thermophysical properties, solidification, undercooling phenomena, phase transformations, and stability of metastable phases in metallic alloy systems[1)].

One of the first samples processed was a ternary steel alloy with nominal atomic composition Fe-21Cr-19Ni representing the family of industrially-cast austenitic alloys. Experiments were aimed at certifying facility operational mode capabilities and conducting calibration tests for various hardware and subcomponent settings. Thus the facility was configured to test the breadth of facility operation and not focused on a specific measurement protocol; however, some science was accomplished albeit under conditions not optimized for science return. This paper summarizes the key findings from these preliminary experiments, compares the results to pre-flight microgravity and ground-based test results, and discusses implications for future materials science MSL-EML experiments in space.

2. Background

The National Aeronautics and Space Administration (NASA) sponsored Electromagnetic Levitation Flight Support for Transient Observation of Nucleation Events (ELFSTONE)[2)] project looks at how melt convection influences phase selection during rapid solidification. Magnetohydrodynamic (MHD) modeling is used to quantify convection during containerless processing of reactive molten samples[3,4)]. In order to conduct this modeling activity, key thermophysical properties must be known as a function of temperature[5)]. Thus, the NASA ELFSTONE team collaborates with the ESA ThermoLab[6,7)] project in order to measure the properties of the exact sample of interest under conditions identical to those used for nucleation studies – same sample, same time span, same conditions, and same facility. Thus thermophysical property measurements are vital to the control of the on-orbit experiments.

2.1 Levitation Techniques

There are many types of containerless levitation processing techniques used in the study of highly reactive molten metal alloys. Only two of these methods are considered here: ElectroStatic Levitation (ESL) and ElectroMagnetic Levitation (EML).

2.1.1 Electrostatic Levitation

The principles of operation for ESL are based on attaining containerless processing conditions by applying a strong static electric field to levitate a charged sample. The droplet is actively held in the field using a complex positioning algorithm

1 Mechanical Engineering Department/Tufts University, 200 College Avenue, Medford MA 02155 USA
2 Institut für Mikro- und Nanomaterialen/University of Ulm/Albert-Einstein-Allee 47, D-89081 Ulm Germany
(E-mail: douglas.matson@tufts.edu)

and sample thermal control is accomplished by laser heating. The result is decoupling of the heating and levitation functions during processing. For ESL processing, the key attributes include processing in an ultra-high vacuum (UHV) environment to limit electrode arcing (high pressure ESL testing is not yet mainstream), processing of conductive and non-conductive samples, and use of small sample sizes, on the order of 50 milligrams, to minimize the required levitation force (with the added advantage that surface deformation is reduced). Changes in sample composition must be monitored due to selective evaporation of key alloying constituents[8]. Induced convection is limited during free-cooling but during heating Marangoni convection may develop due to the presence of surface thermal gradients.

2.1.2 Electromagnetic Levitation

The principles of operation for EML testing are based on attaining containerless processing conditions by applying high frequency alternating currents to water-cooled copper coils to generate magnetic fields which induce a complementary field in a conductive sample. The two fields oppose each other and the droplet is passively held in an electromagnetic potential well. Electrical currents are generated within the sample causing induced internal heating. In both EML facilities described in this work, the sample is positioned by imposing a 150 kHz quadrapole field and heated simultaneously by superimposing a 350 kHz dipole field applied to the same coil system (known by the acronym SUPOS for superposition). Sample thermal control is accomplished either by active gas cooling or manipulation of the magnitude of the applied heating field. The result is a coupling of the heating and levitation functions during processing. For EML processing, the key attributes include processing over a wide range of gas pressures including UHV, selection of conductive samples due to the requirement that internal electric fields are generated, and use of large sample sizes, on the order of 1 gram, to limit evaporation. Positioning-forces can cause significant surface deformation while the induced heating-field can cause significant convection.

2.2 Experiment Categories

There are two major categories of experiments that are run as part of the international collaborations leading to EML experiments on the ISS: Undercooling experiments and Thermophysical Property Measurements.

Undercooling experiments involve thermally cycling the liquid sample below the equilibrium melting point of the parent material to access metastable phases during rapid solidification. The influence of convection on nucleation phenomena, growth kinetics, phase selection and metastable phase formation are investigated. Often, quenched novel microstructures can be returned to earth for subsequent analysis. An example of this type of experiment is seen in **Fig. 1** where growth during solidification of an Fe-21Cr-19Ni sample undercooled 110 degrees below the alloy melting point was imaged using high-speed digital cinematography on the ISS using the MSL-EML facility during video calibration tests. The cool liquid appears grey against a dark background because the molten samples are hot and self-illuminate under proper video aperture settings. Two solid phases are seen growing into the liquid. The outer metastable ferritic phase grows into the liquid and the inner stable austenitic phase grows into the mushy-zone formed during primary solidification. The solid phases appear lighter, because for comparable emissivity hotter is brighter and the stable phase melting point is higher than that of the metastable phase.

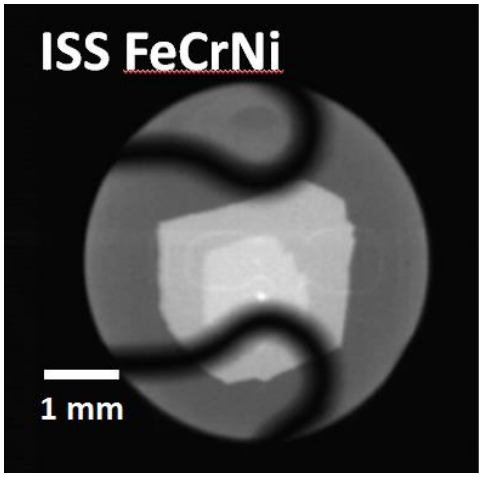

Fig. 1 Phase selection during ISS undercooling tests.

Thermophysical property measurement involves exciting the sample to probe system response as a function of known sample temperature. The most commonly investigated material properties using containerless levitation processing are density[10], thermal expansion[11], surface tension[11], viscosity[12], heat capacity[13], emissivity[14], and electrical resistivity[15]. Only the first four are considered in this paper.

3. Facility Descriptions

3.1 Ground-based Electrostatic Levitation Facility

The NASA Marshall Space Flight Center (MSFC) electrostatic levitator[16] was used to measure FeCrNi thermophysical properties in support of the ELFSTONE project. **Figure 2** shows the exterior of the chamber, details of the lower levitation and positioning electrodes and an image of a heated sample during melting. Density and thermal expansion test methods involve heating the sample with a single radial laser, with significant associated Marangoni convection, and immediately turning the laser power off to limit evaporation losses. The sample is

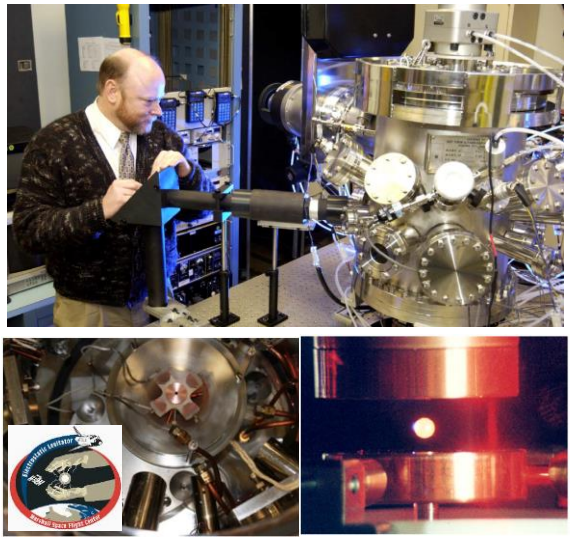

Fig. 2 MSFC/ESL – photos courtesy of NASA.

back-lit using LED lighting in order to project a shadow of the image onto a high-speed digital imaging system while the sample cools; temperature is monitored using one-color pyrometry. Images taken from a side view at 25 frames/second and a resolution of 512x512 pixels; they are correlated to sample temperature through video time-stamps. The exterior surface shape is fit using an edge-detection algorithm such that the volume may be calculated by assuming axial symmetry. By tracking sample mass as a function of time the density can be readily evaluated.

Surface tension and viscosity test methods involve melting the sample and then reducing the laser power to obtain a desired constant temperature and balance radiative thermal losses. A typical thermal profile is shown in **Fig. 3**. The sample also often spins and thus the equatorial region is preferentially

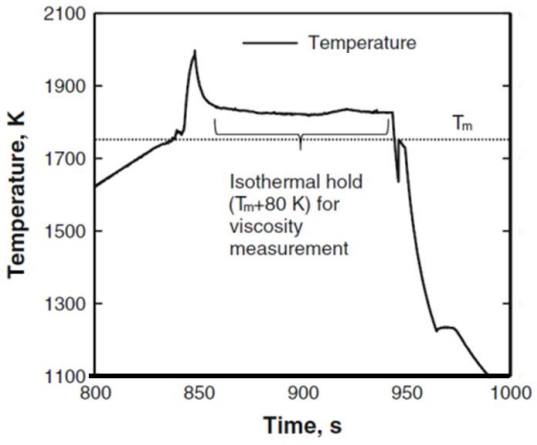

Fig. 3 Isothermal hold during oscillation excitation for ESL surface tension and viscosity testing.

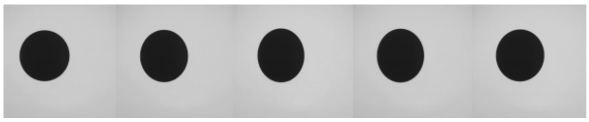

Fig. 4 Mosaic of frames showing back-lit side view images during ESL testing at MSFC.

heated while the poles remain cooler – on the order of several degrees. Marangoni convection develops because the surface tension is higher at the poles, where the temperatures are slightly lower, and surface motion induces internal fluid flow. At the melting point of the FeCrNi ternary steel alloy the maximum flow within the droplet is calculated to be on the order of 0.04 m/sec[17]. Due to the complexity of the levitation control algorithm, the sample is marginally unstable and sudden changes to the field are not possible. Thus, once thermal equilibrium has been reached, the positioning field is oscillated with low amplitude near to the natural frequency for excitation of axial surface deformation. For 40 – 60 milligram FeCrNi samples this was observed to be between 150 – 200 Hz depending on sample mass. Backlit side-view digital images with an acquisition rate of 1000 frames/second and a resolution of 512x512 pixels are used to define sample projected area and dynamic polar diameter – either of which can be used to evaluate the frequency and the rate of oscillation decay required for surface tension or viscosity measurement, respectively. In the series of images shown in **Fig. 4** the sample has minimum height/maximum width in the first and last frames while the middle frame shows maximum height/minimum width corresponding to mode 2 spherical deformation seen from the side. Note that it takes time to excite the natural frequency at a given temperature and thus testing must be accomplished during the isothermal hold. Mixed-mode oscillations are common due to interference between the excitation signal and sample positioning algorithm. To combat this, several tests can be run in sequence during the hold by setting the camera mode to allow multi-triggered data acquisition.

3.2 Electromagnetic Levitation Adapted for Use on Parabolic Aircraft

Parabolic trajectory flights using the TEMPUS facility[18] (German Space Agency (DLR) acronym for Tiegelfreies Elektromagnetisches Prozessieren Unter Schwerelosigkeit or Containerless Electromagnetic Processing under Weightlessness) aboard the Airbus A300 "Zero-G" aircraft was conducted outside Mérignac, France, in September 2013[19] on the FeCrNi alloy. This provided reduced gravity EML containerless test opportunities, as seen in **Fig. 5**, over durations of less than 25 seconds[20] with up to six 1-gram samples processed sequentially during the 30 parabolas scheduled in atypical day. Since run time is limited, in order to complete a full melt cycle while

Fig. 5 ESA parabolic aircraft and TEMPUS flight operations – photos courtesy of ESA and DLR.

maintaining a molten droplet stable during microgravity conditions the sample is preheated to just below the melting point, or approximately 1000 °C, while solid. As soon as the specimen is free-floating, power is increased to induce melting and subsequent superheating of the liquid. Preheating and melting is done in a 20 mbar atmosphere of Argon using the SUPOS coil system. At the desired superheat the chamber is flooded with Helium to a pressure of 300 mbar and the power is reduced to induce cooling at a rate ranging between 25 – 70 degrees/second depending on the heater setting. During cooling the induced convection is on the order of 0.03 – 0.20 m/sec[3]. Nominal gas purity is < 1 ppm O_2 and H_2O.

A typical parabolic aircraft time-temperature profile is presented in **Fig. 6** where the green line represents the microgravity level, the red line represents the heater control voltage, and the grey line represents the positioner control voltage, and the blue represents the sample temperature. The observed temperature spikes represent false readings introduced by the presence of surface oxides on the solid sample, with a correspondingly higher emissivity, which dissolve into the superheated liquid following melting. These oxides represent contamination introduced during the preheating process by

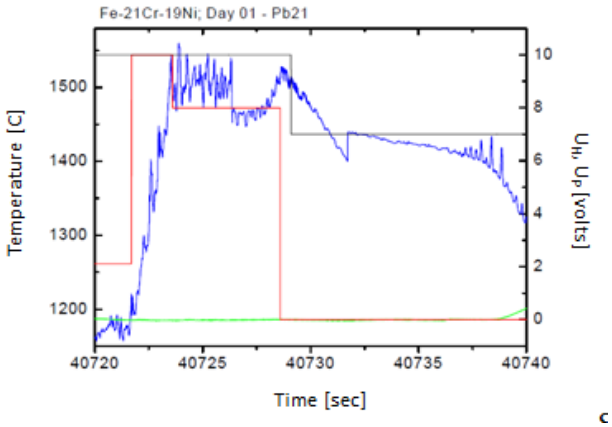

Fig. 6 Typical thermal profile during TEMPUS processing of undercooled FeCrNi.

contact of the hot specimen with the sample holder base. Post-test analysis shows that oxygen is still limited to less than around 20 ppm.

Density measurements are rarely conducted due to flight turbulence which causes significant g-jitter. Undamped sample launch off the holder base causes minor residual sample motion within the positioning field. This creates transient asymmetric surface deformations that lead to significant error when attempting to extrapolate sample volume from areal projections.

Since the sample is stable within the coils a single excitation pulse can be applied using the heater field to induce radial forces that excite mode 2 oscillations which are visualized with high speed digital imaging from the top (axial) at 150 Hz using a Loglux model i5CL camera and the side (radial) at 200 Hz using a Vision Research Phantom V7.3 camera both at a resolution of 256x256 pixels. Camera specifications and operating conditions are the same as used in ISS testing. Multiple pulses can be applied during a single thermal cycle but since the temperature is changing with time these measurements can span the entire range from superheated to undercooled conditions. Even with controlled excitation, mixed-mode oscillations are common due to g-jitter as the timing of the pulse may not correspond to a time when the sample is located at the center of the field and forces on the droplet may thus not be radially symmetric. Note that during melting, wild surface deformation is observed and this uncontrolled excitation can often lead to perturbations which dampen, for FeCrNi, over about 3 seconds following melting. These perturbations are highly mixed-mode in nature and excitation of a controlled mode 2 oscillation cannot commence until internal viscous damping is complete.

3.3 Electromagnetic Levitation on the International Space Station

The MSL-EML facility is controlled out of the Microgravity User Support Center (MUSC) at DLR-Köln as shown in **Fig. 7**. Eighteen samples, each weighing around 1-gram, are processed in each batch and batches are scheduled for deployment to the ISS yearly. Since the samples are run using telemetry from the ground, the transmission delay during commanding requires that facility health inspections must be staged and sequential operational steps, although automated, take significant time to be completed. This can result in an acceleration of sample spin which must be damped. With the steel alloys, the low temperature phase transformations exacerbate rotation and translation thus requiring preheating to 1200 °C with subsequent motion damping prior to initiating melting. Testing is usually conducted in Helium or Argon at 40000 Pa (400 millibar) to reduce preferential evaporation of Chromium from the sample which could result in a shift in composition. For these brief initial facility check-out and calibration tests, processing was

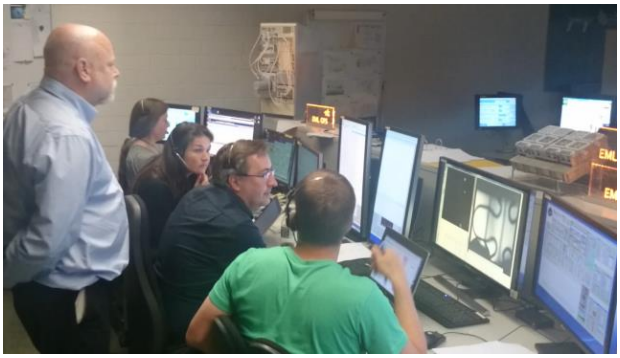

Fig. 7 MUSC Control Room at DLR-Köln.

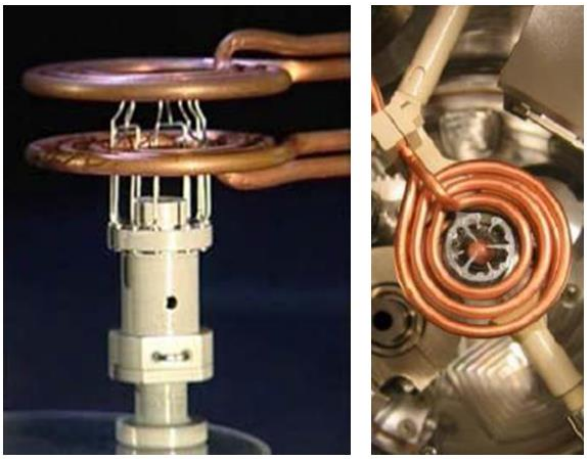

Fig. 8 EML SUPOS coil used to position and heat the sample on the ISS – photos courtesy of Airbus.

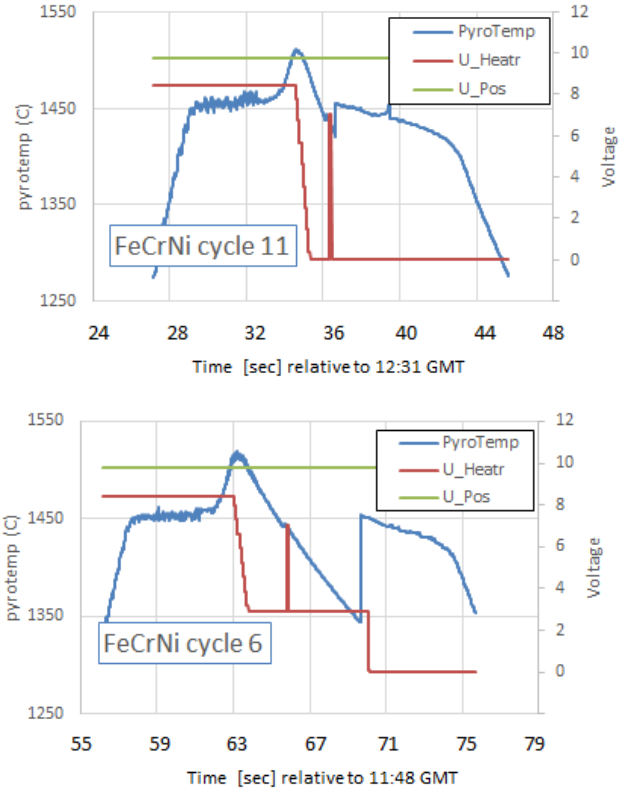

Fig. 9 Triggered oscillations during ISS checkout tests.

conducted at ultra-high vacuum (UHV) on the order of 10^{-6} torr. Sample levitation and heating are done using SUPOS coil system, seen in **Fig. 8**, similar in design to that used on TEMPUS for parabolic flight. Throughout a typical thermal cycle, the positioner power was maintained at the maximum value to maintain sample stability at the coil center and minimize the effects of surface deformation during superheating. During melting, the heater power was maximized and the superheat was restricted to between 50 - 70 degrees above the melting point to minimize evaporation by limiting the time spent as a liquid. The cooling rate could be controlled by setting the heater to reduced values which could also be used to control convection within the droplet during the measurement periods. For example, in the top part of **Fig. 9** a thermal cycle is shown with the heater turned off to achieve maximum cooling, on the order of 50 degrees per second, and minimum stirring, on the order of 0.03 m/sec[3)], a heater pulse was applied to excite mode 2 oscillations for surface tension and viscosity evaluation at the melting temperature. The lower part of the Figure shows a different cycle profile where the heater was reduced to an intermediate value resulting in slower cooling, on the order of 25 degrees per second, and enhanced stirring, on the order of 0.12 m/sec[3)]. Again, the heater was pulsed to excite oscillations at the melting temperature. In both instances, the lack of oxide-induced temperature spiking during melting indicates that the sample surface was clean throughout the tests.

Since the number of cycles is limited in space, undercooling and material property measurement must be accomplished simultaneously and thus when the sample is molten camera settings are optimized such that the steel droplet is self-illuminating. As opposed to what was previously seen for ESL the EML sample (behind the sample holder wires which form the cage top) appears bright against a dark background, as seen in **Fig. 10**. This can make edge detection more difficult as edge pixel contrast is influenced by both view factor and intensity. Although it is difficult to see by eye, the first, third and fifth frames are larger in diameter than the second and fourth.

During a typical MSL-EML run each of the two cameras has two operational modes: data acquisition and facility health. Data acquisition involves triggering by automated on-orbit software. At other times, the default operation is conducted at slower frame rates to limit bandwidth requirements for download; these images are used by the operators to ensure facility health.

Fig. 10 Mosaic of frames showing self-illuminated top view images during EML testing on the ISS with every frame shown at 25 Hz.

The top-view axial camera and pyrometer (ACP) is a Loglux model i5CL nominally set to 384x384 pixels at 150 Hz for viscosity and surface tension measurement. Mode 2 oscillations are seen as projections of circles which cyclically ebb and wane in diameter as seen in **Fig. 10**. For ISS calibration tests the ACP images are stored on the facility hard disk onboard the ISS but for these experiments they were corrupted during download making analysis impossible. Software changes have been implemented to streamline image compression protocols necessary to avoid compromising download bandwidth restrictions and prevent this from occurring in future tests but for these checkout tests most property measurements were successfully extracted from lower quality (reduced acquisition rate) facility health video at 25 Hz.

The radial (RAD), or side-view high speed camera (HSC), is a Vision Research Phantom V7.3 with two lens settings, high speed with 256x256 pixels at up to 60 kHz for recalescence detection and high resolution with 600x600 pixels at 20-1000 Hz for data acquisition during density measurement; recording is on the camera ring-memory buffer. At all other times the default operation was set the near real-time download rate to 15 Hz, at the given lens pixel setting, for facility health monitoring. Since the purpose of these checkout tests was calibration of the recalescence detection software, the RAD was set to 30 kHz and the auto-exposure correction software was turned off to avoid overriding the subtle intensity changes seen in **Fig. 1**. In most instances recalescence occurs long after the excitation is damped as seen in the bottom portion of **Fig. 9** and thus no property information is recorded. The HSV was configured to save only 0.3 seconds of data prior to recalescence triggering, at most capturing 8 oscillations in 9000 frames, which luckily did occur once as part of these tests; this is shown in the top portion of **Fig. 9** where the heat pulse and recalescence are seen to be nearly superimposed. This fortuitous event is displayed in **Fig. 11** with 25 microseconds between each frame showing a single fluctuation (prolate-oblate-prolate) in the series of eight oscillations. The sample is viewed from the side behind the holder cage wires and the mode 2 oscillation behavior is strikingly evident. The polar inclination angle due to either coil offset or inhomogeneity introduced by the coil loop entrance/exit was around 8 degrees. For all other cycles only facility health data is available from the side view and this 15 Hz data is deemed not useful for property evaluation (for a 3 second damping event this is only 45 points making reconstruction of the oscillations impossible).

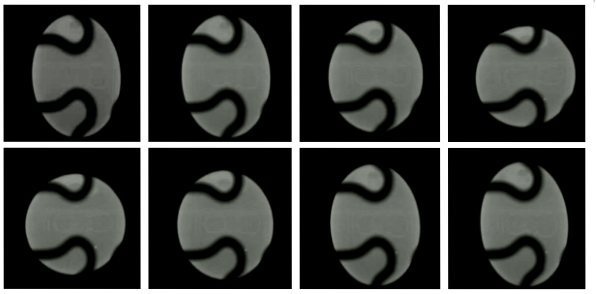

Fig. 11 Mosaic of frames showing selected side-view images from recalescence detection at 30 kHz.

4. Analysis and Discussion

4.1 Density

Density evaluations from two ESL runs are compared to the ISS results in **Fig. 12** (no PF results were possible). Standard regression techniques were used to evaluate variability[21]. The results compare very well in both magnitude and in functional behavior with temperature although the space results were successfully able to access significantly deeper undercoolings than observed using ESL. Previous results on alloys with similar composition are displayed in the figure for comparison.

$$\text{Density} \quad \rho = \frac{m}{V} \tag{1}$$

$$\rho\,\big|_{Tm}^{ESL} = 6984 \pm 2 - 0.712 \pm 0.035\,(T - T_m) \tag{2}$$

$$\rho\,\big|_{Tm}^{ISS} = 6997 \pm 15 - 0.743 \pm 0.316\,(T - T_m) \tag{3}$$

For density, ρ, in [kg/m^3] and temperature, T, in [K] and referenced to the melting temperature T_m = 1720 K.

It is apparent that the reported error bars using the ISS recalescence mode camera setting are higher than the observed scatter for ESL. The most important factor contributing to data scatter is the inherent variability observed during sample calibration which translates into calculations to define droplet volume. Volume is then tracked with time and thus with temperature. For ESL, both calibration (using a precision-ground sample dedicated to this function) and testing (on the hot sample) are conducted using back-lit imaging with high spatial resolution video settings. For the ISS EML, the calibration was conducted using the silhouette of a precision ground Zirconium sample at room temperature while the measurement was done on self-illuminating droplets. Additionally from the top-view back-lighting is not possible and thus edges are more

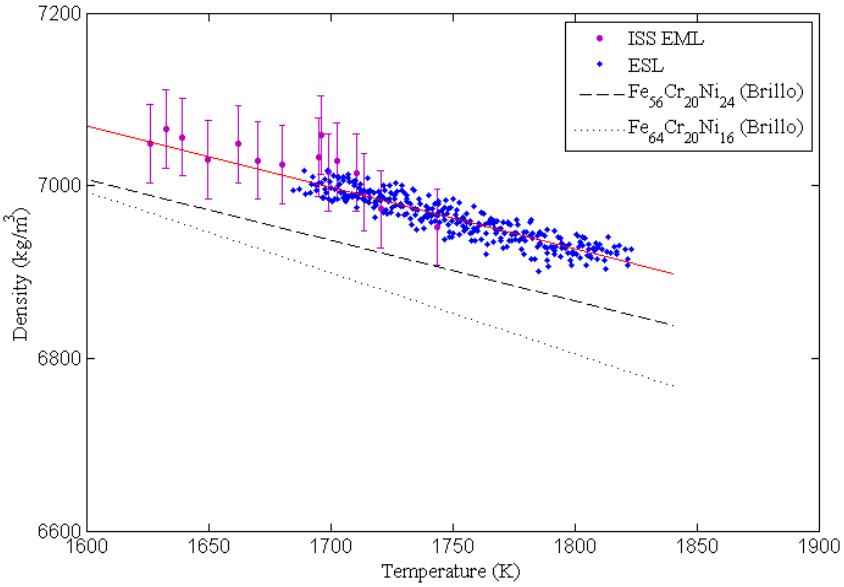

Fig. 12 Comparing ESL and MSL-EML Density Results.

difficult to detect, leading to pronounced variability. These impacts on precision will not change and represents an inherent characteristic of high temperature ISS alloy measurement techniques since it is not feasible to perform calibrations using samples having similar emissive characteristics as a molten droplet. This effect is mitigated during measurement of thermal expansion since the impact on edge detection is minimized as we compare sequential images of the hot sample at one temperature to images at a second temperature with nearly the same emissive characteristics. A secondary effect is use of low spatial resolution radial camera lens setting which also accentuates edge detection noise due to a lower pixel count; subtle sample motion also introduces signal noise. This is an artifact of the configuration selected for checkout testing that allows for recalescence detection; dedicated density runs with both back-lighting and use of the higher resolution camera can easily be run in the future. A third contributor was the limited number of data points run in space. This was not a dedicated run to investigating density. There are 16 data points in space and 310 for ESL. The reduced number of points in space has a significant impact on the reported precision – future tests will not suffer from sample population size limitations.

Note that density was evaluated from the top view in MSL-EML tests and from the side in ground-based ESL. This is important for ESL given that levitation forces to overcome gravity deform the sphere into an oblate spheroid which must be viewed from the side to define volume properly. In space the sample is spherical within measurement error sensitivity. Since levitation forces are reduced, viewing the sample axially is acceptable. Note that in the future the high-resolution lens configuration involves radial viewing.

4.2 Volume Thermal Expansion

Despite the fact that measuring the influence of temperature on volume (and on density) requires comparing relative areas with edges of similar emissive character, to define volumetric thermal expansion we must look at instantaneous slope as seen in Equation 4. Any fluctuation in apparent volume results in a slope which swings from positive to negative values on successive data points. Thus, data regression techniques must be used and key temperatures selected for reporting. In this case, the logical case is at the melting temperature.

Volume Thermal Expansion

$$\beta = \frac{1}{V}\frac{\partial V}{\partial T}\bigg|_T \tag{4}$$

$$\beta\,|_{Tm}^{ESL} = 1.18 \pm 0.13 \times 10^{-4} \tag{5}$$

$$\beta\,|_{Tm}^{ISS} = 1.02 \pm 0.18 \times 10^{-4} \tag{6}$$

Overall precision is defined using propagation of error techniques. Linear regression defines the average volume and slope for thermal expansion in units of [K^{-1}]. Regression also defines the standard deviation for both populations and from this the coefficient of variability (the ratio of the standard deviation to the mean) is used to define the standard deviation of the amalgamated population defined by Equation 4[21]. Note that thermal expansion was observed to be almost independent of temperature over the range investigated which is to be expected for a material exhibiting linear dependence of density with temperature.

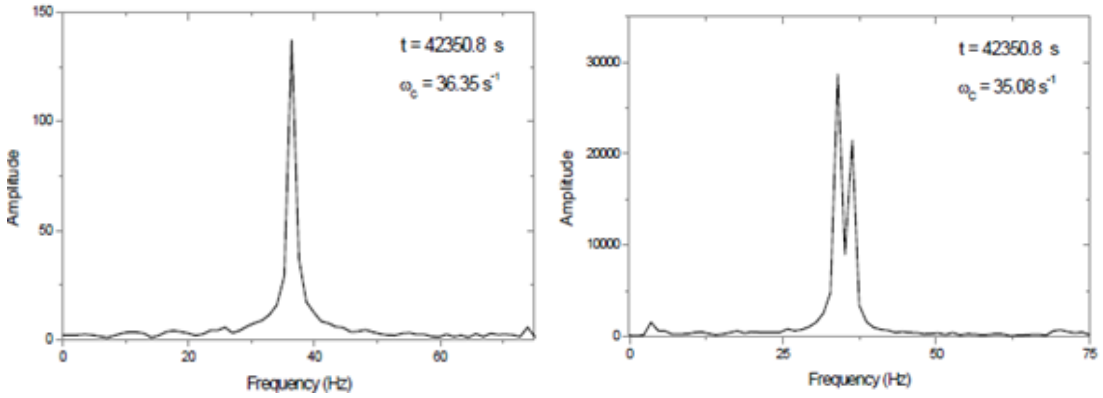

Fig. 13 FFT of oscillation frequencies for PF steel.

4.3 Oscillation frequency measurement

During mission planning, it was thought that use of ISS facility health video would not be possible for property measurement. Data compression issues during download forced a reevaluation of this position. Although property measurement was not the prime objective of these tests, multitasking of efforts enhances productivity and encourages collaboration so an investigation was initiated to look at whether useful information was embedded in the existing record for extraction.

From parabolic flights using a comparable coil with comparable HSV on comparable samples it was seen that due to g-jitter sometimes mode 2 oscillations could be attained and sometimes mixed-mode motion was observed. This is seen in **Fig. 13** where Fast-Fourier Transform (FFT) analysis of the signal reveals a characteristic frequency of between 35-38 Hz. At issue was the configurationally imposed problem of trying to measure a signal with a natural frequency on the order of 35 Hz with a video system set to capture images at an acquisition rate of 25 Hz in space. Fortunately this frequency, and the surface tension derived from it, is a very weak function of temperature and only sample mass was found to have a strong influence on the values observed.

At 25 Hz, the Nyquist limit is 12.5 Hz and to sample a signal at 35 Hz we must rely on undersampling. Using this method, we expect information to be lost. The classic example of undersampling is a scene from an old Western movie where the rotation rate of a slow moving wagon wheel can be imaged by tracking a spoke if the camera frame rate is more than double the spoke superposition frequency. If sampled at less than this rate the wheel may appear to rotate at a rate inconsistent with ground motion – even backwards. By undersampling we have lost information because we know the wheel is moving but we don't know absolutely what the rotation rate is since it could be multiples of the spoke spacing apart. In our case we have an advantage in that we know approximately what the oscillation frequency should be and thus can use the results of undersampling to confirm that this value is consistent with observations and is thus possible. If we know the speed of the wagon and the camera frequency then we can predict at what rate the wheel should appear to spin and confirm this by looking at the film playback. This technique is called Super-Nyquist sampling.

A simulated sinusoidal signal is plotted in **Fig. 14**. The characteristic frequency of the parent signal is 36.6 Hz and the amplitude is arbitrarily reduced to simulate viscous damping. Two conditions are shown – oversampling at 150 Hz with red dots and undersampling at 25 Hz with blue dots connected together to show how beats are formed. The oversampled condition is what is to be expected during nominal property measurement configuration while the undersampled condition is what is to be expected using health monitoring video. The oversampled data fully captures system response but the undersampled condition results in data loss. An FFT of the undersampled simulation is displayed in **Fig. 15** and shows the characteristic frequency of the signal at 11.72 Hz. This signal reflects across the Nyquist limit at 12.5 Hz to form an alias at 13.28 Hz which is manifested as the observed beat with frequency f_{beat} = 13.28 – 11.72 = 1.56 Hz. The high-frequency alias of this signal also represents the lost parent frequency since f_{lost} = 11.72 + 25 = 36.72 Hz[22]. This compares well with the simulation parent signal at 36.6 Hz but a small positive bias, 0.3%, is also introduced using this technique.

4.4 Surface tension

From the analysis of frequency spectrum, the loss of analysis for surface tension measurement is mitigated by knowledge of what frequencies are expected and the ability to eliminate aliased signals. Based on this approach, the surface tension, γ, was calculated based on the frequency, f, mass, m, and mode $l=2$ with results displayed in **Fig. 16**:

$$\gamma = \frac{3\pi m}{l(l-1)(l+2)} f^2 \qquad (8)$$

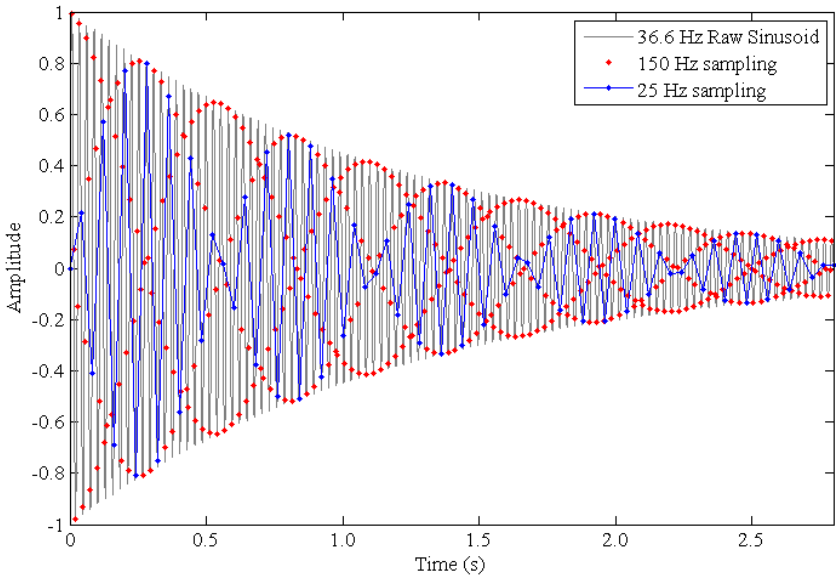

Fig. 14 Simulated decaying sinusoid signal at 36.6 Hz with oversampling at 200 Hz and undersampling at 25 Hz.

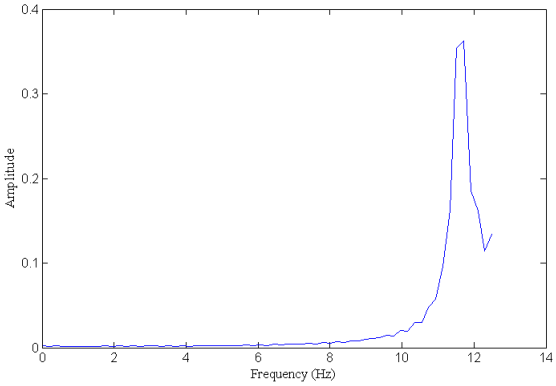

Fig. 15 FFT to the Nyquist limit of 12.5 Hz for simulated undersampled data at 25 Hz from a parent sinusoidal signal at 36.6 Hz.

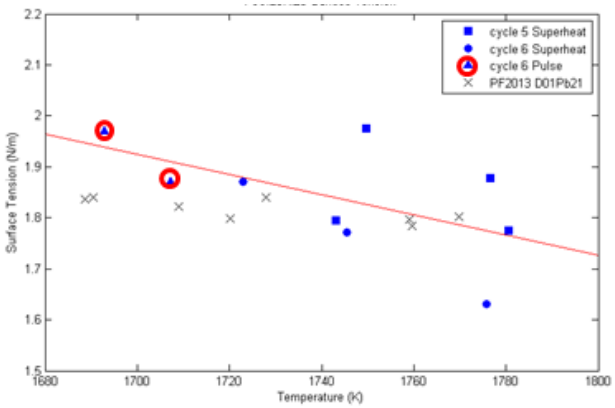

Fig. 16 Surface tension for FeCrNi steel.

In the Figure the ISS data is shown as colored symbols and the parabolic flight data is shown as a series of gray X's. Note that two data points were also extracted from the 30 kHz imaging run with very low associated error. All frequencies observed were in agreement with observations during parabolic flight validating the techniques used. There is significant scatter at high temperatures due to mixed-mode excitation from turbulence during melting. This can be seen in **Fig. 17** by looking at a typical oscillation where the deformation amplitude is plotted as a function of time after reaching maximum superheat. The signal is quite clean for pure mode-2 oscillations induced by the application of the heater pulse and imaged at 30 kHz but mixed mode components significantly distort the oscillations imposed by melt convection. This shows that analysis of un-pulsed data is not recommended.

4.5 Viscosity

The loss of information for viscosity evaluations is different than that for surface tension analysis. From our wagon-wheel analogy, the wheel may appear to go backwards but it doesn't change diameter. But in our system the signal amplitude does change with time and we can use the beat to our advantage. In **Fig. 18**, the beat maximums correspond to the true signal values. We can evaluate the decay time, τ, from beat maximum to beat maximum and measure the viscosity, μ, from density, ρ, and sample radius, R_o, using the relationship

$$\mu = \frac{\rho R_o^{\,2}}{(l-1)(2l+1)\tau} \tag{9}$$

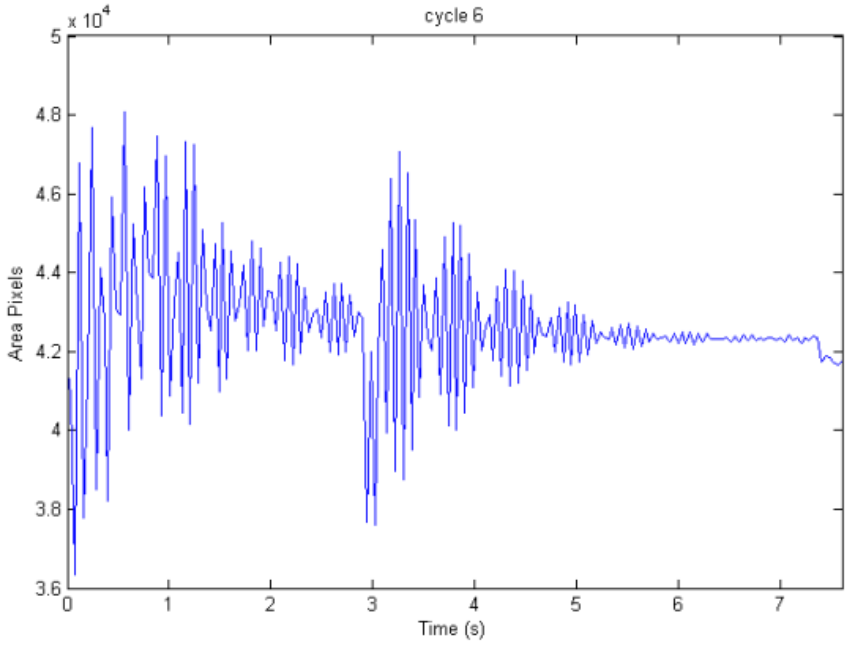

Fig. 17 Typical oscillation intensity for MSL-EML steel; first pulse envelope from melting excitation, second from applied deformation.

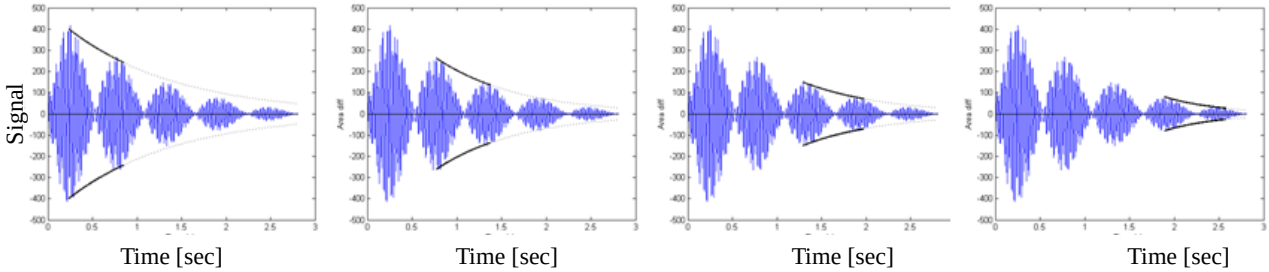

Fig. 18 Decay measured between successive beats; four temperature ranges are defined by five beats.

What is lost is temporal resolution of the signal. The original signal could involve resolution to 36.6 Hz but we are able to obtain measurements only at 1.8 Hz as seen in **Fig. 18**. The temperature is changing with time and thus the error bars on measurement temperature are significantly larger. We get the correct value but not as often. This is seen in **Fig. 19** where the brown symbols are from ground-based ESL, the gray x's are from parabolic flight TEMPUS EML, and the blue symbols are from ISS MSL-EML. Note that the spread in ESL data is mainly due to potential mixed-mode excitation at constant temperature while the error in ISS data is due to an extended temperature range from beat analysis. PF data error is not quantified because it was difficult to define when mixed-mode excitation occurred even though the temporal resolution was better than in space and the aliasing beat was eliminated.

5. Conclusions

Side image analysis is not useful for surface tension or viscosity but is useful for density – but only with the high spatial resolution lens configuration. Ground density results appear to have a higher precision with use of back-lighting and silhouette edge detection. Care must be exercised when calibrating the on-orbit cameras during density measurement due to the desire to investigate self-illuminating samples; this does not affect surface tension or viscosity measurements.

During the first 3 seconds after superheating, the sample exhibits strong mixed-mode deformation which introduces significant error. The sample should fully dampen before application of an excitation pulse.

Undersampling can be used but some loss of information occurs. For surface tension this involves confirming a known sample oscillation frequency to remove signal alias biasing. For viscosity this involves a reduction of the temporal resolution of the measurement resulting in an increase in the magnitude of temperature error bars. Although side view 15 Hz health monitoring video is not useful for property measurement, if the 150 Hz top signal is temporarily lost the 25 Hz signal can be

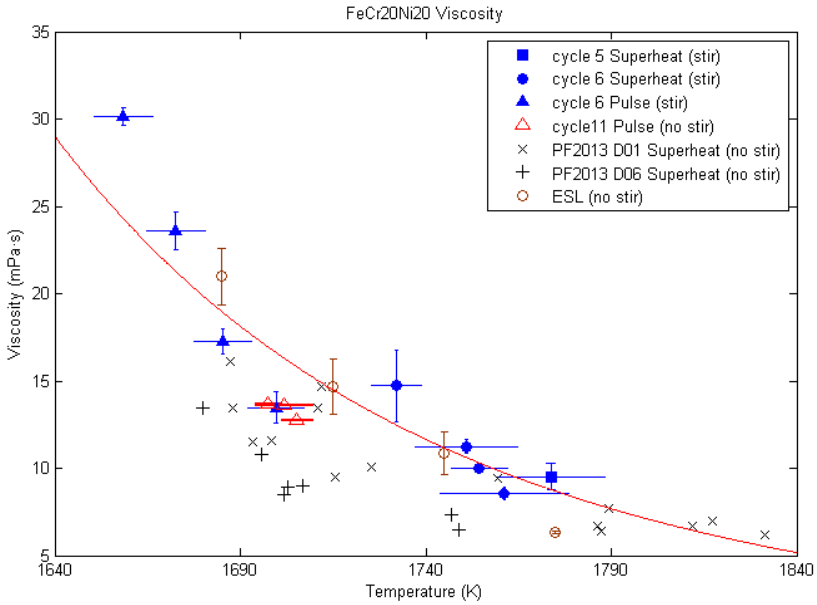

Fig. 19 Viscosity for FeCrNi steel.

used to fill in the data. In these instances, alias identification is readily accomplished using Super-Nyquist sampling.

Numerical comparison of results on ground using MSFC-ESL, on parabolic flight using TEMPUS, and in space using MSL-EML show no significant difference in accuracy for density, thermal expansion, surface tension or viscosity measurements. Precision is reduced in space due to the use of sub-optimal sampling rates imposed by facility configuration settings that support validation and calibration testing and by the limited number of data points taken during checkout tests. When the facility is reconfigured for future property measurement it is certain that improvements will be realized.

Acknowledgements

Funding supporting this work was provided by NASA under Grant Number NNX16AB59G, by DLR under contract 50WM1170 and by the ESA MAP Project *Thermoprop* AO-99-022 and AO-2009-1020 Contract Number 4200014306. The authors would like to thank the various facility operations personnel – from NASA/MSFC ESL, Mike SanSoucie, Trudy Allen, and Glenn Fountain; from DLR TEMPUS, David Heuskin, Stephan Schneider, Stefan Klein, and Georg Lohöfer; and from ESA MSL-EML, Angelika Diefenbach, Stephan Schneider, Sandra Schumann, Julianna Schmitz, Brigitte Pätz, Marcus Engelhardt, Jim Volp (ESA-EDR), and Wolfgang Soellner (Airbus).

References

1) A. Seidel, W. Soellner and C. Stenzel: J. Physics Conf. Ser., **327** (2011) 012057.
2) D.M. Matson, R.W. Hyers, T. Volkmann and H.-J. Fecht: J. Physics Conf. Ser., **327** (2011) 012009.
3) J. Lee, X. Xiao, D.M. Matson and R.W. Hyers: Met. Trans. B, **46** (2015) 199.
4) J. Lee, D.M. Matson, S. Bi nder, M. Kolbe, D. Herlach, and R.W. Hyers: Met. Trans. B, **45** (2014) 1018.
5) D.M. Matson, AIAA-2012-0592 (2012).
6) H-J. Fecht and R.K. Wunderlich: Proc. 1st Int. Symp. Micrograv. Res. Appl. In Phys. Sci. & BioTech. ESA SP, **454** (2001) 545.
7) H-J. Fecht, in Topical Teams in the Physical and Life Sciences-Towards New Research Applications in Space ESA SP, **1281** (2005) 24.
8) J. Lee and D.M. Matson: Int. J. Thermophys., **35** (2014) 1697.
9) J. Lee, J.E. Rodriguez, R.H. Hyers and D.M. Matson: Met. Trans. B, **46** (2015) 2470.
10) H. Yoo, C Park, S. Jeon, S. Lee and G.W. Lee: Metrologia, **52** (2015) 677.
11) I. Egry, G. Lohoefer and G. Jacobs: Phys. Rev. Lett., **75** (1995) 4043.
12) T. Ishikawa, P-F. Paradis, J. Okada and Y. Watanabe: Meas. Sci. Technol., **23** (2012) 025305.
13) H-J. Fecht and W.L. Johnson: Rev. Sci. Instrum., **62** (1991) 1299.
14) T. Ishikawa, Y. Ito, J.T. Okada, P-F. Paradis, Y. Watanabe and T. Masaki: Meas. Sci. Technol., **23** (2012) 125602.
15) G. Lohöfer and G. Pottlacher: High Temperatures-High Pressures **40** (2011) 237.
16) J.R. Rogers and M. P. SanSoucie: Proc. 50th AIAA, Nashville TN Jan 2012, AIAA , 2012-0924.
17) M.C. Flemings, D. M. Matson, W. Löser, R. Hyers, and J. Rogers: SRD for LODESTARS, NASA Document LODESTARS-RQMT-0001 (2003).
18) A. Diefenbach, G. Lohofer, W. Dreier, and J. Piller: Proc. 53th Int. Astro. Congress, Houston TX Oct 2002, IAC-02-J.5.03.
19) D. Heuskin and S. Schneider: Experiment Performance Report, PF23-MUSC-EML-RP001, DLR, Köln Germany (2013).
20) R. Aune, L. Battezzati, R. Brooks, I. Egry, H.-J. Fecht, J.-P. Garandet, K.C. Mills, A. Passerone, P.N. Quested, E. Ricci, S. Scheider, S. Seetharaman, R.K. Wunderlich, and B. Vinet: Microg. Sci. Tech., **16** (2005) 11.
21) R.G. Budynas and J.K. Nisbett: Shigley's Mechanical Engineering Design, McGraw-Hill, New York, **20** (2008) 992.
22) W.H. Press, B.P. Flannery, S.A. Teukolsky and W.T. Vetterling: Numerical Recipes, The Art of Scientific Computing, Cambridge University Press, NY (1986) 386.